AD NUMBER
ADB012032
LIMITATION CHANGES

TO:

Approved for public release; distribution is unlimited.

FROM:

Distribution authorized to U.S. Gov't. agencies only; Test and Evaluation; 02 JUL 1976. Other requests shall be referred to U.S. Army Missile Command, Redstone Arsenal, AL 35809.

AUTHORITY

AMC ltr, 8 Sep 1976

ENGINEERING DESIGN FOR ADVANCED ADDS

FINAL TECHNICAL REPORT
APPENDICES

AVCO RESEARCH AND SYSTEMS GROUP

January 5, 1976

Contract No. DAAH01-75-C-0976

prepared for

HEADQUARTERS
U.S. ARMY MISSILE COMMAND
Redstone Arsenal, Alabama 35809

ATTN: DRCPM-HEL

14 *AERL-75-773-App.*

ENGINEERING DESIGN FOR ADVANCED ADDS *Appendicies.*
9 FINAL TECHNICAL REPORT
APPENDICES

15 *DAAH01-75-C-0976.*

AVCO RESEARCH AND SYSTEMS GROUP
2385 Revere Beach Parkway
Everett, Massachusetts 02149

11 *5 Jan 76*

12 *48 p.*

048450 dn

TABLE OF CONTENTS

LIST OF ILLUSTRATIONS

APPENDIX A

P&T MOTIONS

APPENDIX A

P&T MOTIONS

$T = J\alpha = 5000\,(2)$

$\qquad = 10000^{-11\#}$

$\alpha = \dfrac{T}{K_\Theta}$

$K_\Theta = 4Kr^2 \text{ (rotational)}$

$K = W^2M \text{ (linear)}$

$\qquad W = 2\pi f_h$

$\qquad f_h = \text{isolator frequency - cps (lateral)}$

$K = (2\pi f)^2 \dfrac{5000}{386}$

$K_\Theta = 4\,(2\pi f)^2 \dfrac{5000}{386} \cdot r^2$

$\alpha = T\left[(4)\,(2\pi f)^2 \dfrac{5000}{386} \cdot r^2\right]^{-1}$

$\alpha = 10000\left[2045.5\, f^2 \cdot r^2\right]^{-1}$

$\alpha = \dfrac{4.8887}{f^2\, r^2}$

$\ddot{\alpha} = 2\,\text{RAD/SEC}^2$

$I \cong 5000\ ''\#\,\text{SEC}^2$ (AZ)

$W \cong 5000^{\#}$
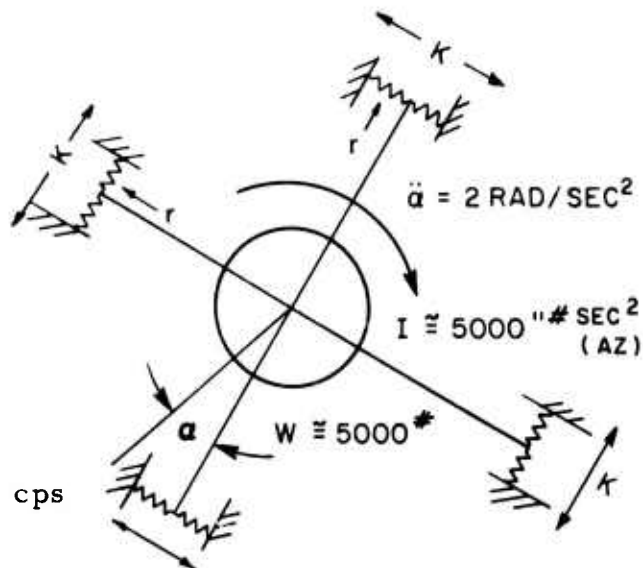
Examine α for 1, 10, 20 and 100 cps systems. Let r vary from 18" (D = 36") to 100". This assumes that lateral uncoupled isolation frequency of P/T system would be in the 8 - 15 cps range since 1 cps would be too soft and 100 cps is in the structural range and much too stiff for practical isolation purposes.

A-3

TABLE A-I

RADIANS — AZIMUTH

r'' f_h(cps)	1	10	20	100
18	.015	.00015	3.75×10^{-5}	1.5×10^{-6}
36	.00375	3.75×10^{-5}	$.9375 \times 10^{-5}$	3.75×10^{-7}
50	.00195	1.95×10^{-5}	4.875×10^{-6}	1.95×10^{-7}
100	.0004885	4.885×10^{-6}	1.22×10^{-6}	4.885×10^{-8}

Clearly, assuming reasonable values of radius geometry r (inches) and isolation system resonance, ($\leq$ 36" and $\leq$ 10 cps) the rotational displacements start to approach $100\,\mu$ radians which is marginal with respect to pointing and tracking correction capability. Figure A-1 is a plot of Table A-1, above. In the elevation planes, the situation is also similarly bad since the center of gravity of the pointing and tracking system would be high with respect to the horizontal mounting plane of the isolators. This situation occasions coupled "rocking modes" which result from coupling of the lateral uncoupled resonance with the torsional natural frequency, resulting in low-frequency sway.

ρ = radius of gyration

$$= \sqrt{\frac{I_M}{M}}$$
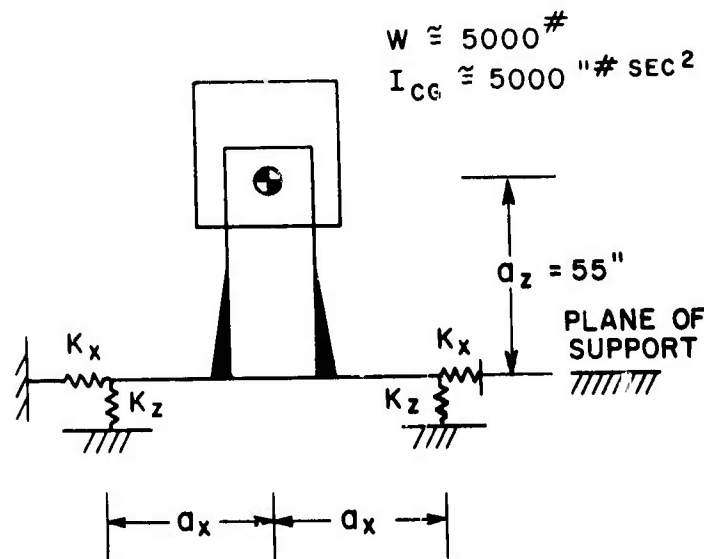
$$I_M = I_{cg} + M a_z^2$$

$$= 5000 + \frac{5000}{386} (55)^2$$

$$I_M = 44184''\#sec^2$$

$$\rho = \sqrt{\frac{44184}{5000}} (386)$$

$$\rho = 58''$$

$W \cong 5000^\#$

$I_{CG} \cong 5000$ "$\#$ SEC^2

$a_z = 55"$

PLANE OF SUPPORT

K_x K_z K_x K_z
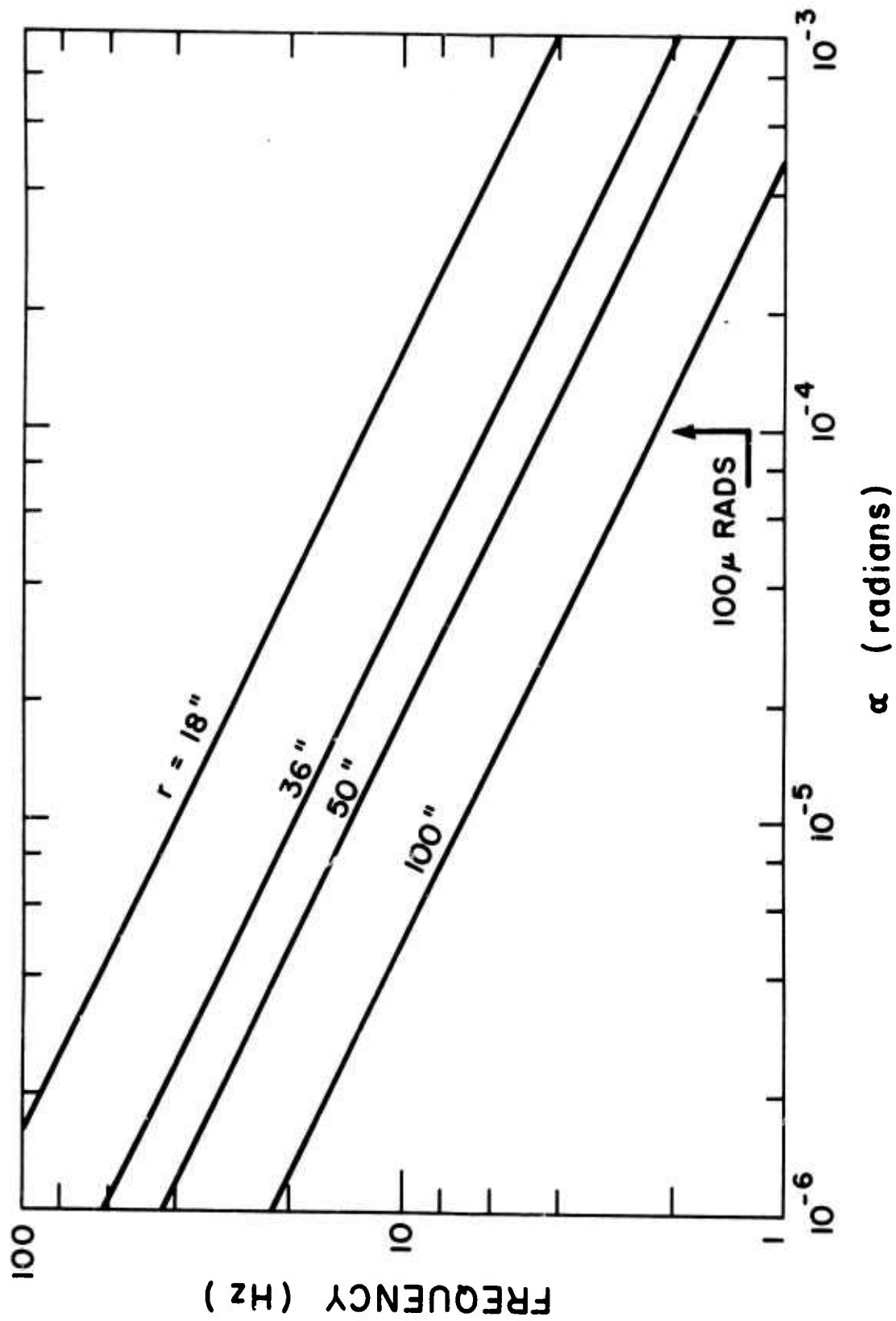
a_x a_x

The solution to the frequency equation is as follows:

Figure A-1   P&T Rotation

$$\frac{f_{coup}^2}{f_z^2} = \frac{1}{2}\left[\frac{K_x}{K_z}\left(1+\frac{a_z^2}{\rho^2}\right)+\frac{a_x^2}{\rho^2} \pm \sqrt{\left[\frac{K_x}{K_z}\left(1+\frac{a_z^2}{\rho^2}\right)+\frac{a_x^2}{\rho^2}\right]^2 - 4\frac{K_x}{K_z}\frac{a_x^2}{\rho^2}}\right]$$

where f_{coup} are the two (2) rocking frequencies and f_z is the vertical trans-
lational resonance (see "Shock and Vibration Handbook", Chapter 3-21,
Harris & Crede).

(U)   Now let us assume the following: The ratio $K_x/K_z = 1$ (horizontal to
vertical stiffness ratio of isolators) and that $a_x = 18"$ ($\approx$ P&T radius at base)
which is a minimum or conservative value.

(U)   Solving for f_{coup} when $f_z = 20$ cps (the designed vertical translational
resonance)

$$f_{coup}^2 = \frac{1}{2}(f_z)^2\left[1\left(1+\frac{55^2}{58^2}\right)+\frac{18^2}{58^2} \pm \sqrt{\left[1\left(1+\frac{18^2}{58^2}\right)+\frac{18^2}{58^2}\right] - \frac{4(18)^2}{58^2}}\right]$$

$$f_{coup}^2 = 200 \quad 1.8992 + .0963 \pm 1.8965$$

$$f_{coup} = 4.45 \text{ cps and } 27.9 \text{ cps.}$$

Note that the 4.45 cps is quite low and is characterized by a rocking mode
which has as its center of rotation a point somewhat below the plane of the
isolators. Assuming this radius is $r = a_z = 55"$, the angular rotation as-
sociated with this resonance and 4 rad/sec^2 angular acceleration can be cal-
culated as follows: The moment of inertia of the telescope portion of the
P&T about the elevation axis $I_{el} = 700^{11\#sec^2}$ and assuming a maximum
angular acceleration of $\ddot{a} = 2$ rad/sec^2, the torque is

$$T = I_{el}\ddot{a}$$
$$= 700 (z) = 1400^{11\#}$$

This torque must now act on the entire inertia of the P&T system about the
center of rotation ($r \tilde{=} a_z$)

$$I_o = I_{cg} + Ma_z^2$$

$$= 5000 + \frac{5000}{386}(55)^2$$

$$I_o = 44183.9^{11\#sec^2}$$

$I_{eL} = 700 " \#$

$M = 5000^\#$
$I_{co} \cong 5000 " \# SEC^2$

a_z

"O"
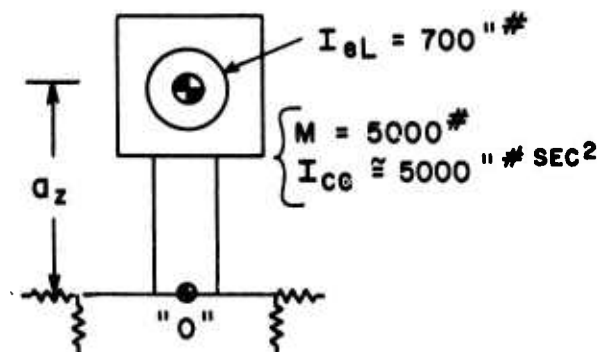
$$\ddot{a} = \frac{T}{I_O} = \frac{1400}{44183.9} = .0317$$

$$\ddot{a} = .0317 \text{ rad/sec}^2$$

$$a = \frac{\ddot{a}}{W^2} = \frac{.0317}{(2\pi 4.45)^2} = 40 \mu \text{ radians}$$

which is approaching the limit of P&T corrective optics systems (100μ rad).

It should be noted that there is a system of decoupling these modes to eliminate the low rocking frequency and still utilize vibrational isolators. Essentially this method depends on relocating the plane of the isolator elastic axes such that the c.g. of the mounted body falls in that plane. Thus by definition, any lateral inertia load produced at the center of gravity can only result in translational motion.

The method requires that the isolators be inclined at some angle which is a function of K_x/K_y, the horizontal-to-vertical stiffness ratio, a_z, the c.g. location, and a_x, the distance $(1/2)$ between isolators. There are very definite limits to the above parameters which if exceeded preclude decoupling.

The system is quite sensitive to the above parameters and much simpler to analyze than to apply to actual hardware and should be avoided if possible in critical applications.

A second approach is to apply "torsional restraints" in the form of special hardware such as tie rods, special springs, etc., all of which are cumbersome, heavy and of questionable value in actual mounting systems.

The above have been noted as possible alternatives should "soft mounting" of the P&T system become necessary as the result of excessive vibration responses (angular rotations).

APPENDIX B
HIGH ENERGY ELECTRON SCATTERING

APPENDIX B

HIGH ENERGY ELECTRON SCATTERING

A. MULTIPLE ELECTRON SCATTERING THROUGH A FOIL

Electron transport through a single slab has previously been treated in great detail, (B-1) so we will only briefly outline the theory. For a beam of electrons uniform in the x and y directions, striking a plane parallel plate that has a thickness t in the z-direction, the Boltzmann equation can be written as

$$\mu \frac{\partial f}{\partial z} = N \int \{ f(z, \underline{u}') - f(z, \underline{u}) \} \sigma(\mu_0) \, d\underline{u}' \tag{B-1}$$

where μ is the cosine of the angle between the electron trajectory and the z axis, μ_0 is the cosine of the angle between the incident and scattered electron trajectories and $\underline{u}$ is the unit vector in the direction of the electron motion.

Expanding the distribution function and the scattering cross section as a sum of Legendre polynomials:

$$f = \sum_{\ell} A_\ell P_\ell(\mu) \tag{B-2}$$

and

$$\sigma = \sum_{\ell} \sigma_\ell P_\ell(\mu_0) \tag{B-3}$$

Substituting expansions (B-2) and (B-3) into Eq. (B-1) and making use of both the orthogonality relation and addition theorem for Legendre polynomials, Eq. (B-1) becomes

$$\left(\frac{\ell}{2\ell-1} \right) \frac{\partial A_{\ell-1}}{\partial z} + \frac{(\ell+1)}{(2\ell+3)} \frac{\partial A_{\ell+1}}{\partial z} + 2\pi N A_\ell \int_{-1}^{+1} d\mu \sigma(\mu) [1 - P_\ell(\mu)] = 0 \tag{B-4}$$

The scattering cross section is, of course, the screened Rutherford that is modified to include relativistic effects and inelastic scattering by orbital electrons. Relativistic effects for small Z, i.e., Z < 27, can be included by use of the McKinley-Feshbach expansion of the complete Mott formulas. Assuming the Thomas Fermi atomic model, the screening angle η is given by

$$\eta = \frac{1}{2} \frac{h}{p} \left[\frac{1.12 Z^{1/3}}{0.885 \, a_0} \right]^2$$

B-1. Jacob, J.H., Phys. Rev. **A8**, 226 (1973).

where p is the momentum of the electron and a_0 the Bohr radius. Making the following substitutions

$$G_\ell = 2\pi N \int_{-1}^{+1} d\mu\, \sigma(\mu) \left[1 - P_\ell(\mu)\right]$$

$$\frac{1}{\lambda} = \frac{G_1}{2} = \frac{\pi N Z(Z+1)}{p^2 v^2} e^4 \left\{ \ln(1+1/\eta) - \frac{1}{1+\eta} + 2\pi\, a\beta - (\beta^2 + \pi a\beta) \right\} \qquad (B-5)$$

Where λ is the transport mean free path, $\xi = z/\lambda$ and $a = Z/137$. Equation (B-4) can then be rewritten as

$$\frac{\ell}{2\ell-1} \frac{\partial A_{\ell-1}}{\partial \xi} + \frac{(\ell+1)}{(2\ell+3)} \frac{\partial A_{\ell+1}}{\partial \xi} + \frac{2G_\ell}{G_1} A_\ell = 0 \qquad (B-6)$$

   Equation (B-6) forms an infinite set of coupled differential equations with constant coefficients. To obtain a solution for the scattering through a slab the boundary conditions at each surface have to be included. Consider an electron beam of arbitrary but known distribution function impinging on a target thickness t. Hence at $\xi = 0$, $f(\mu \geq 0, \xi = 0)$ is known and at the far boundary $\xi = t/\lambda$ there are no particles entering the target, hence $f(\mu \leq 0, \xi = t/\lambda) \equiv 0$. The above boundary conditions can be written as

$$f(\mu \geq 0, \xi = 0) = \sum_{n=0}^{\infty} b_{2n+1}\, P_{2n+1}(\mu)$$

and

$$f(\mu \leq 0, \xi = t/\lambda) = \sum_{n=0}^{\infty} c_{2n+1}\, P_{2n+1}(\mu) \equiv 0$$

$$(B-7)$$

   In Eq. (B-7) use has been made of the fact that the odd Legendre polynomials form a complete set in the half space. This choice is by no means unique; one could, for example have chosen the even polynomials. However, as the current is a more readily measurable quantity than density, odd polynomials are used. Thus there is an infinite set of boundary conditions at each surface, but because of the truncation there are only $N+1$ unknowns. Hence, we specify $(N+1)/2$ conditions at each boundary. Making use of orthogonality, one has Marshak's boundary condition

$$\int_0^1 d\mu\, P_{2n+1}\, f(\mu, \xi = 0) = \frac{b_{2n+1}}{4n+3}$$

and

$$\int_{-1}^0 d\mu\, P_{2n+1}\, f(\mu, \xi = t/\lambda) = 0$$

$$n = 0 \ldots \frac{N}{2} \qquad (B-8)$$

B-4

Figure B-1 shows the emergent distribution function of electrons after having passed through a 1/2 mil aluminum foil for electron energies of 200 keV, 150 keV and 100 keV. The angle at which the distribution function falls to half its value is 17° for 200 keV electrons, 27° for 150 keV electrons and 50° for 100 keV electrons.

The above analysis assumes that the electron energy is strictly a constant. This is clearly not the case. We can allow for energy variation by dividing the slab into many layers and allowing the electron energy to vary from one layer to the next. At the free surfaces the boundary conditions are given by Eq. (B-8), while at the interface $Z = Z_1$, we assume that there is no discontinuity in the distribution function as one goes from one layer to the next. This continuity can be insured by setting

$$A_{\ell 1}(Z_1) = A_{\ell 2}(Z_1) \qquad \ell = 1, 2 --- N$$

where $A_{\ell 1}$ and $A_{\ell 2}$ are the coefficients of the ℓth Legendre polynomial in the two layers.

Energy loss is included assuming that the electron continuously loses energy as it penetrates the material. The effects of straggling are neglected. The path length of most of the electrons will be greater than the thickness of the target considered because of elastic scattering. To a first approximation it is assumed that only elastic scattering exists. The resulting angular spread of the electrons can be computed and hence the average electron trajectory. The target is divided into a number of thin layers and in each layer we assume that the energy loss is given by

$$\Delta w = \left(\frac{dw}{dS}\right) \langle S \rangle \tag{B-9}$$

where w is the electron energy and dw/dS is the Bethe stopping power given by

$$\frac{dw}{dS} = \frac{2\pi e^4}{mc^2 \beta^2} \frac{N_a \rho}{A} Z \left\{ \ell n \left[\frac{T^2 (T+2)}{2 (I/mc^2)^2} \right] + 1 - \beta^2 \right.$$

$$\left. + \left[T^2/8 - (2T+1) \ell n^2 \right]/(T+1)^2 \right\} \tag{B-10}$$

where N_a is Avagadro's number, A the atomic weight, T the kinetic energy of the electron in units of the electron rest energy and I is the mean excitation energy. For I we have used the values recommended by Berger.[B-2] $\langle S \rangle$ is the average path length of the electron in the given slab and it is given by

$$\langle S \rangle \approx \frac{t}{\langle \cos \Theta \rangle} \tag{B-11}$$

where t is the slab thickness and $\langle \cos \Theta \rangle = 1/2 (\langle \cos \Theta \rangle_1 + \langle \cos \Theta \rangle_2)$, $\langle \cos \Theta \rangle_1$ and $\langle \cos \Theta \rangle_2$ being the average value of μ at the beginning and end of each slab for the particles traveling in the positive μ direction only. This

---

B-2. Berger, M.J. and Seltzer, S.M., NAS-NRC Publication No. 1133 (1964) (unpublished).
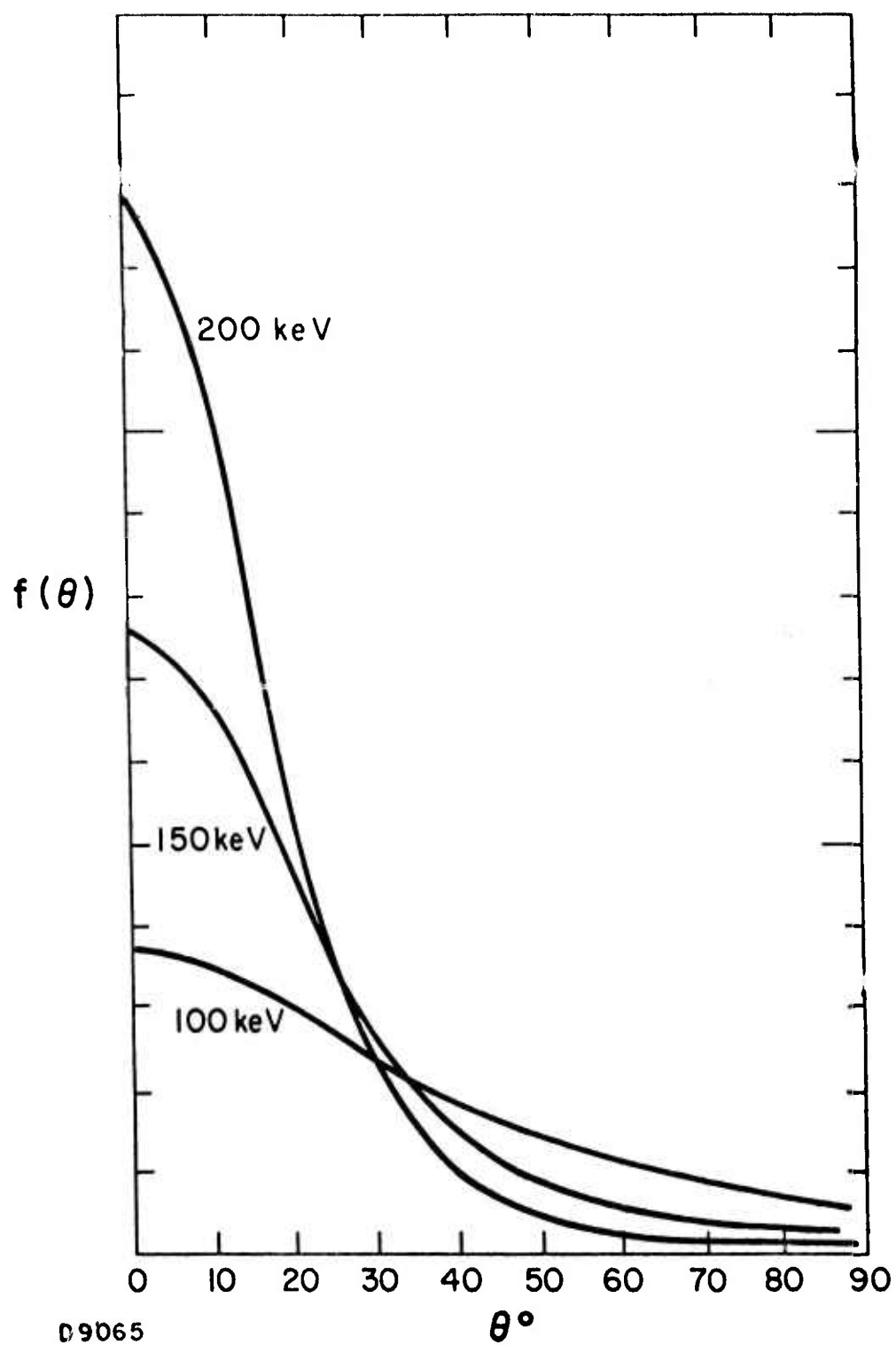
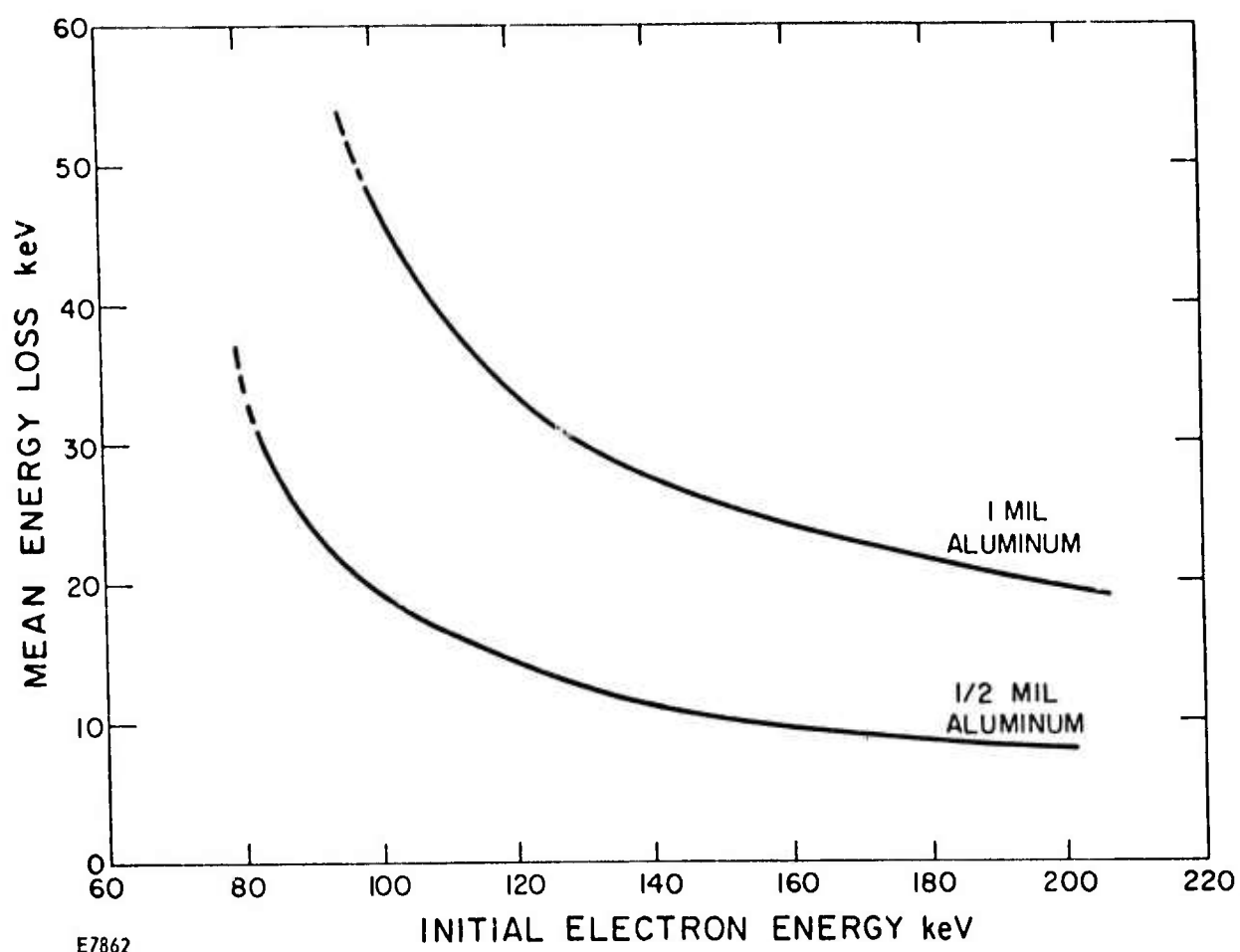Figure B-1   Emergent Electron Distribution Function

Figure B-2   Plot Electron Energy Lost as a Function of Initial
Electron Energy for a 1/2 and 1 mil Al Foil

ignores the backscattered particles (in computing the average path length only). The error so introduced is expected to be small, however, if the thickness of each layer is much less than λ, the transport mean free path. The multi-layer theory also neglects the absorption of electrons. Because of these approximations it has been found convenient to connect the multi-layer theory to the age diffusion theory. The age theory is just the P_1 approximation with the inclusion of energy loss. We have extended the age theory to include effects of an applied electric field.

Results using the above analysis are presented and discussed below. Figure B-2 shows the mean energy lost by a collimated beam of electrons striking 1/2 and 1 mil aluminum foil. So if one subtracts the energy loss from the initial electron energy one obtains the mean energy of the electrons after traversing the foil. If one is interested in using kapton, the curves in Fig. B-2 are also useful because a kaptan foil of thickness t has the same energy loss as an aluminum foil of thickness $t/2$.

APPENDIX C

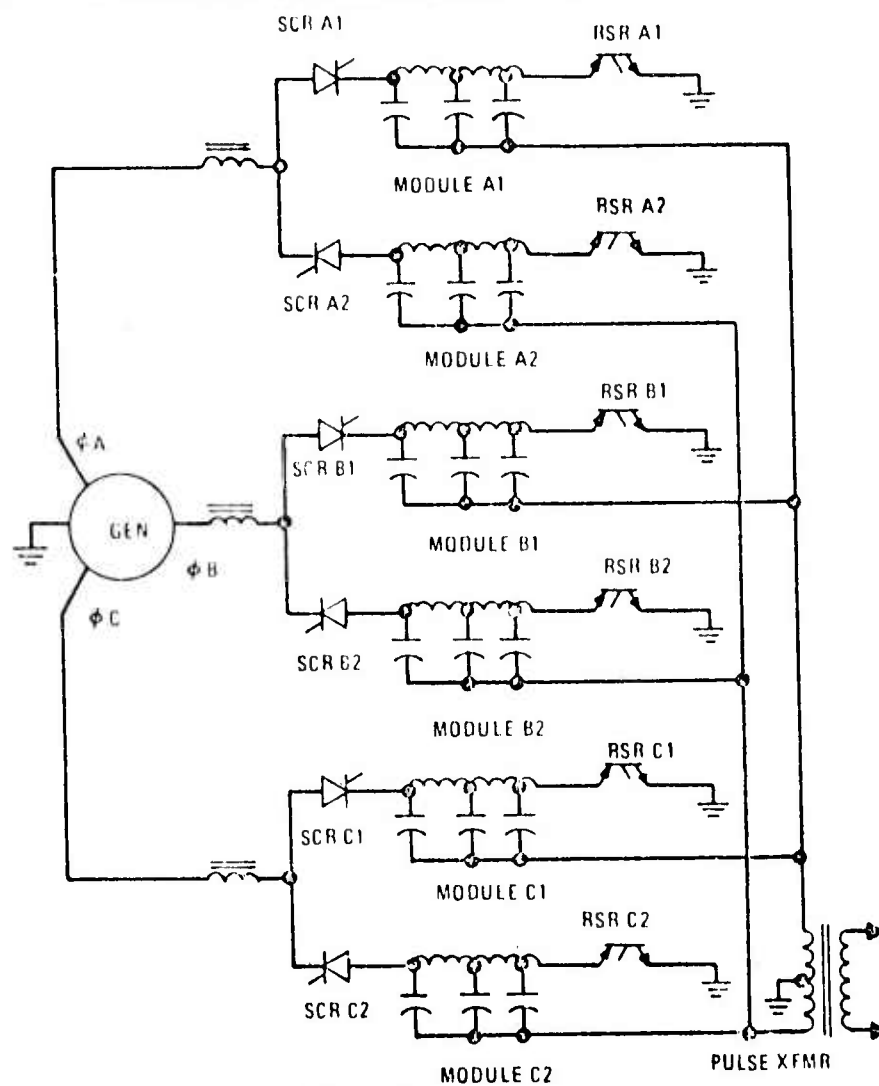AC RESONANT CHARGING PRINCIPLES

(WESTINGHOUSE)

APPENDIX C

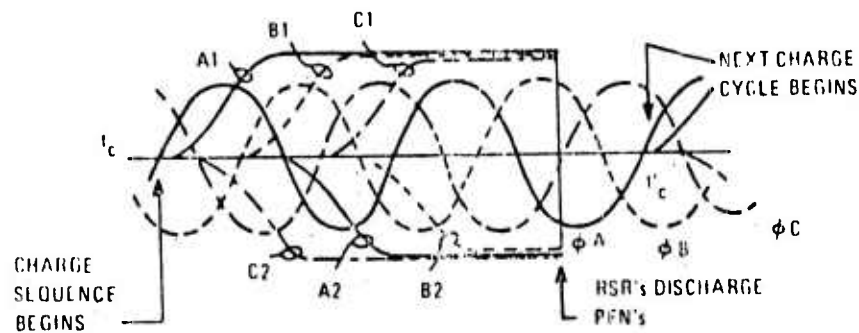## AC RESONANT CHARGING PRINCIPLES

A. Basic 3-Phase Modulator

Figure C-1 is a simplified schematic and waveform diagram for a basic Advanced RSR Modulator system which illustrates the essentials of circuit operation. The basic circuit includes a three phase generator as prime electrical power source and six PFN-switch modules, one for each polarity of each phase of the generator. The outputs of the six modules are combined and transformed to the required voltage by the output pulse transformer.

The time sequence of PFN charging and pulse discharge is illustrated by the waveforms in Figure C-1b. The time t_c indicates the beginning of the PFN charging sequence. In the basic circuit, SCRs act as controlled charging diodes for the PFNs. The charging sequence begins with the triggering of SCR A1 at t_c. PFN A1 then charges during the half cycle of phase A immediately following t_c. In sequence, SCR C2 is triggered 60° later followed by B1, A2 and so on. The charging cycle ends upon completion of charging of PFN B2.

Discharge of the six PFNs through the pulse transformer to the load occurs when the six RSR switches are triggered simultaneously. Because PFN charging occurs during both positive and negative half cycles of line voltage, three of the six PFNs are charged positively and three negatively. Therefore, the output pulse transformer is center-tapped and connected in a manner to combine all module outputs in the proper polarity.   C-3

(A) CIRCUIT DIAGRAM

(B) PFN VOLTAGE WAVEFORMS

Figure C-1 AC Resonant Charging Circuit

C-4

The output of the basic pulser circuit is a repetitive pulse sequence whose pulse repetition frequency (PRF) is a sub-multiple of the generator frequency. In the basic example in **Figure C-1, a second** charging sequence can begin at time t_c' which follows t_c by two cycles. Therefore, if the generator is a 400 Hz generator the highest output PRF is 200 pulses per second (pps), that is one pulse every two cycles of line frequency. Time t_c' can be delayed for three cycles after t_c, in which case the PRF is 133 pps. Longer delays result in lower PRF.

B. AC Resonant Charging

AC resonant charging, illustrated in **Figure C-2**, is a particular method of capacitor charging from an AC source in which a series inductance is chosen to resonate with the capacitance at the AC source frequency. **The circuit in Figure C-2a consists of an AC voltage sourse,** an SCR, a charging inductance and the capacitance to be charged. The charging cycle for full resonant charging begins with triggering of the SCR as the source voltage passes through zero in a positive going direction. **The waveforms in Figure C-2b illustrate the resulting charging** response. The charging cycle ends as the capacitor voltage reaches its peak and the capacitor attempts to discharge back into the generator through the SCR.

The waveforms in Figure C-2b show the full resonant case in which current flows for 180° to charge the capacitance to $\pi/2$ times the peak value of the source voltage. For this case, the expressions for charge voltage and current are:
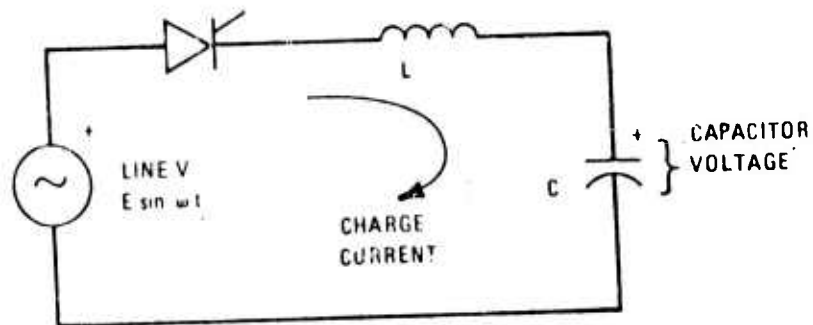
(A) CIRCUIT
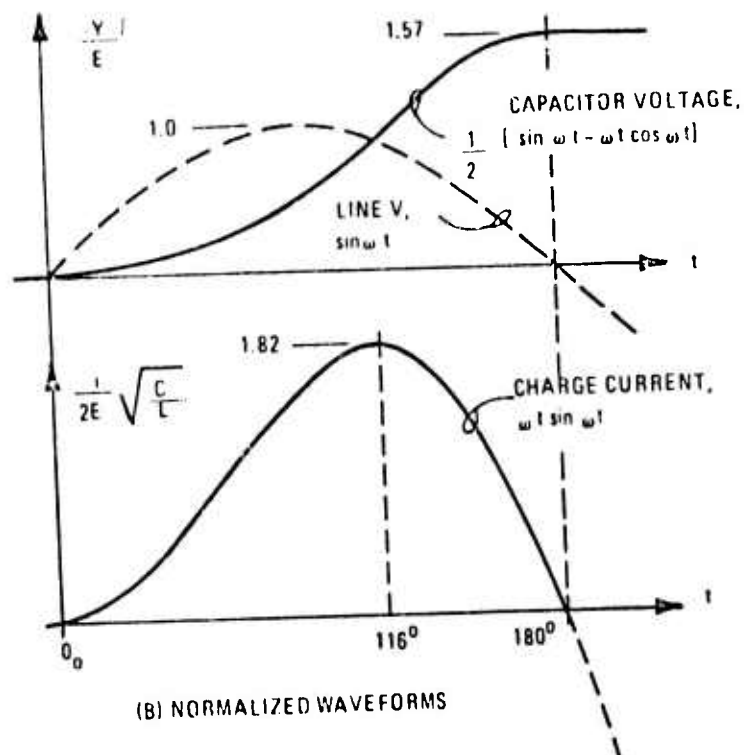
(B) NORMALIZED WAVEFORMS

Figure C-2 AC Resonant Charging

$$v(t) = \frac{E}{2} \left\{ \sin \omega t - \omega t \cos \omega t \right\}$$

$$i(t) = \frac{E}{2\sqrt{\frac{L}{C}}} \; \omega t \sin \omega t$$

respectively, where E is the peak voltage of the source sine-wave, ω is the line frequency and circuit resonant frequency in radians per second.

Within limits, if the circuit in Figure C-2 is resonant at some frequency different from the source frequency, the capacitor charges to a different voltage over a different conduction angle. Figure C-3 is a plot of peak capacitor voltage as a function of the circuit resonant frequency and the corresponding conduction angle at which the capacitance is fully
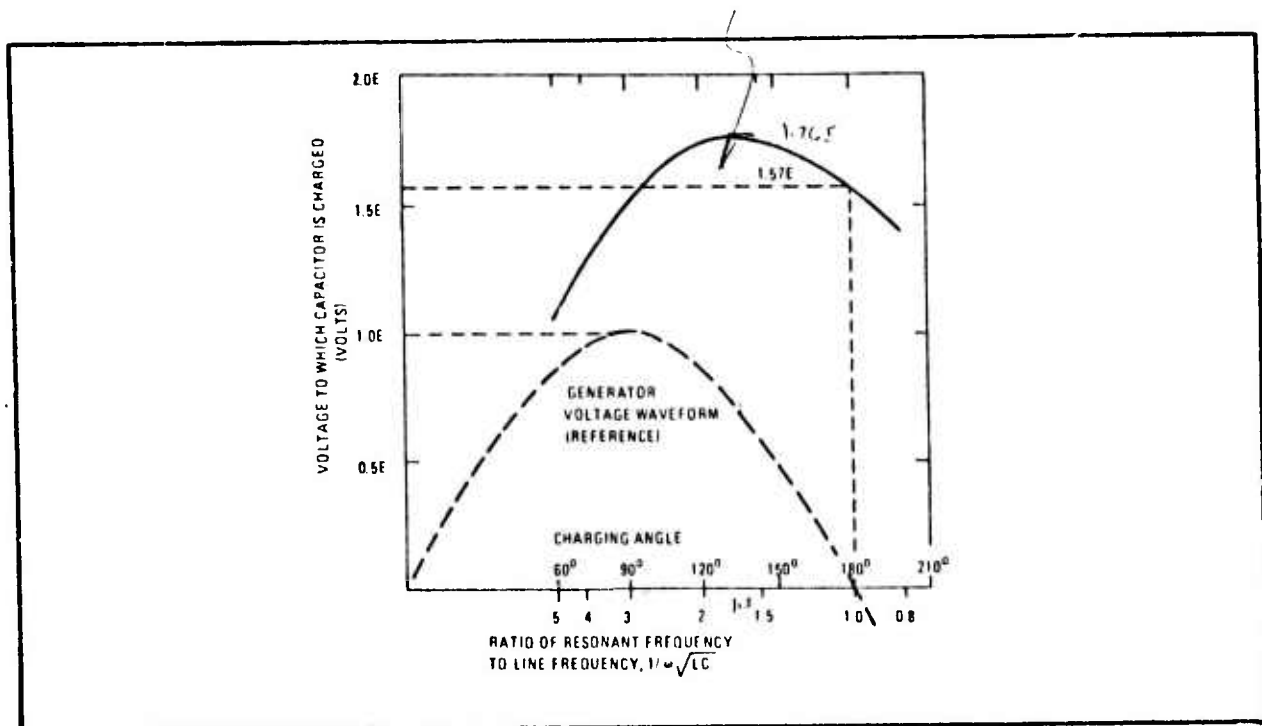

Figure C-3 AC Resonant Charging Voltage as a Function of Circuit Resonant Frequency

charged. The general expressions for capacitance coltage and charging current in this more general case are:

$$v(t) = \frac{E}{1 - \omega^2 LC} \left\{ \sin \omega t - w\sqrt{LC} \ \sin \sqrt{\frac{1}{LC}} \ t \right\}$$

$$i(t) = \frac{E}{\frac{1}{\omega C} \left[1 - \omega^2 LC \right]} \left\{ \cos \omega t - \cos \sqrt{\frac{1}{LC}} \ t \right\}$$

The expressions indicate that charging can be accomplished all the way down to a conduction angle of about 60°. At lower angles, voltage on the capacitor rises to E by 90° of the line voltage waveform.

(U)   In general, this charging concept is useful for angles of from 90° to 180°. Maximum voltage on C is 1.76E, achieved at 135° with $\frac{1}{\omega \sqrt{LC}} = 1.3$. However, in the interest of minimizing the harmonic content of the charging current in the generator, full cycle or resonant charging is preferred.

C. Multimodule System

The expansion of the basic six module system into a multimodule system is illustrated in Figure C-4. This system uses three phase and N modules per phase; therefore, the total number of modules is 3N. If ϕ phases were used, the number of modules would then be ϕN.

The charging sequence is programmed so that one module at a time is charged from each line. Therefore, the entire charging sequence requires a number of operating cycles of the generator. A typical charging sequence and waveforms from one phase are illustrated in Figure C-5. The total per pulse energy out of this three phase system
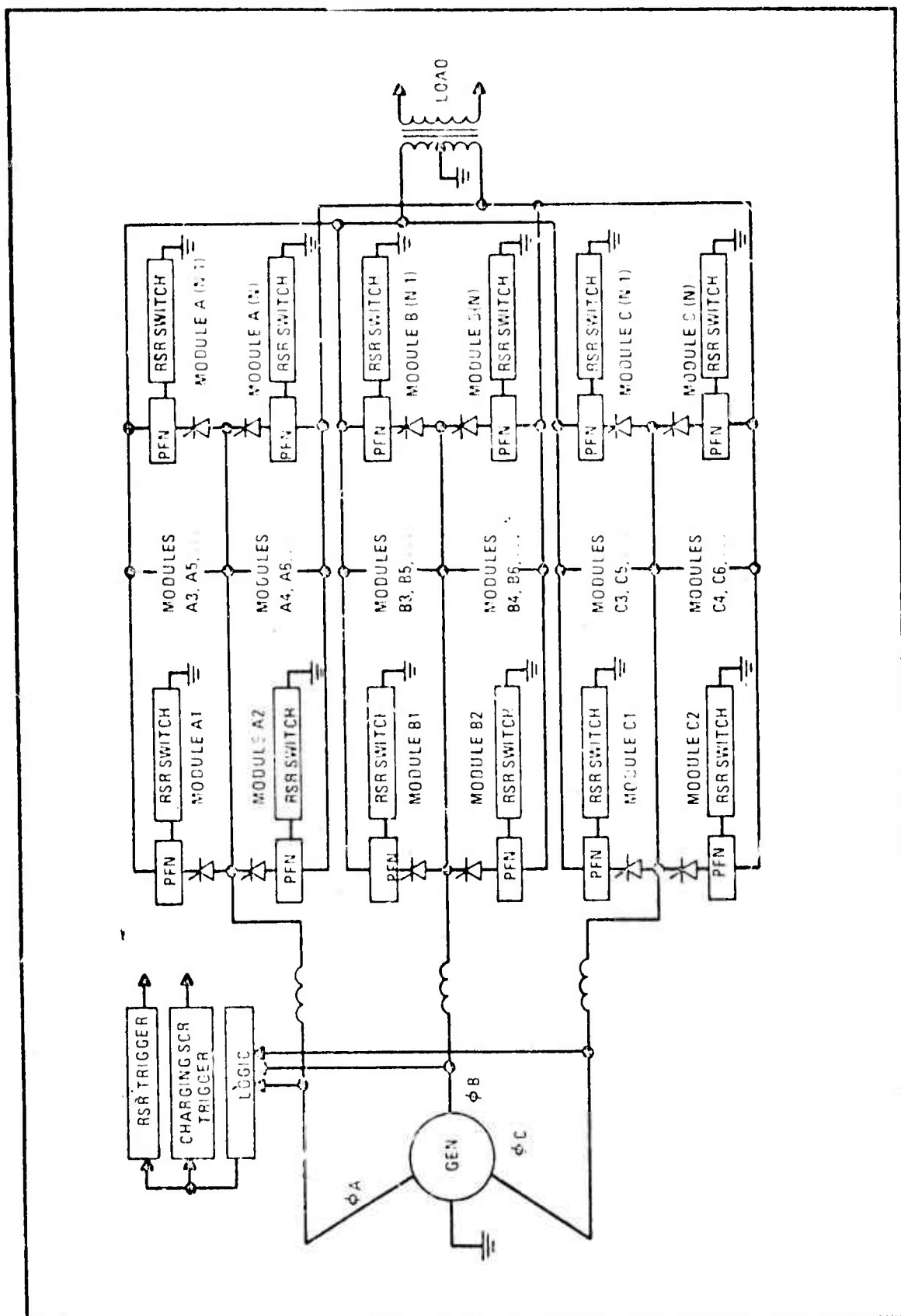
Figure C-4 Multimodule, Three-Phase AC Resonant Charging
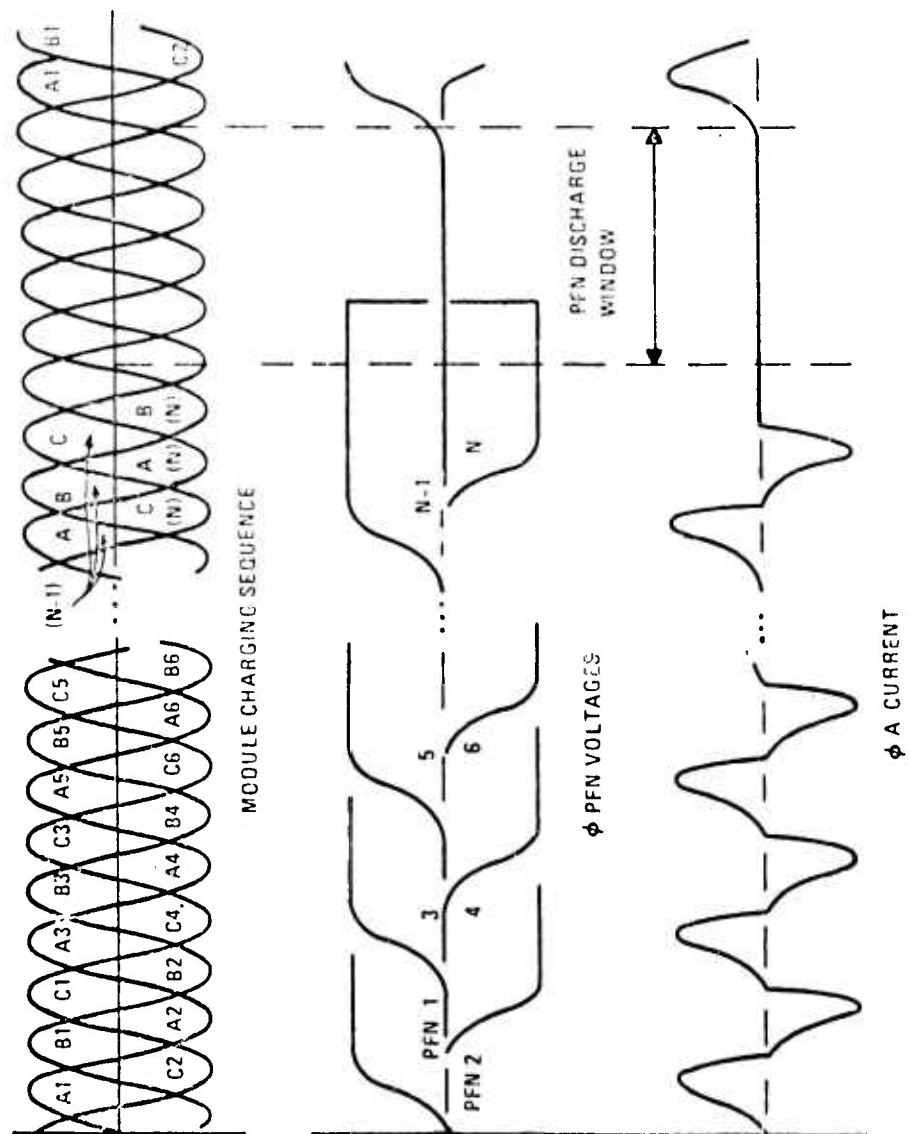
Figure C-5 Multimodule, Three-Phase AC Resonant Charging Waveforms

is 3N times the stored energy per module. Storage voltage per module is $\pi/2$ times the peak line-neutral voltage of the AC source.

A key consideration in this approach is the relationship between PRF and the generator frequency f_g. For the six module system, maximum PRF is $f_g/2$. For the multimodule system, with each module charged in sequence, the maximum PRF is $2 f_g/(N + 2)$, where N is the number of sequentially charged modules per phase. This frequency can be increased by charging more than one module at a time. It is important to note that with this approach, the PRF of the pulser is related to the generator frequency.

APPENDIX D

8-MW ALTERNATOR DESCRIPTION

(AiResearch)

APPENDIX D

8-MW ALTERNATOR DESCRIPTION

The alternator is a wound-field synchronous type machine having a round or nonsalient pole rotor construction with distributed excitation (field) windings. The rotor does not incorporate damper windings, but the solid non-salient pole rotor core structure does act to provide damping effect. The horizontally mounted alternator is intended to be driven at 12,500 rpm from a high-speed gas turbine through a suitable gearbox. Incorporated into the alternator assembly are two ancillary rotating exciters, a rotating recti-fier assembly, an output voltage control unit, and various instrumentation provisions. By virtue of its ancillary excitation provisions, the alternator is a completely self-excited and brushless unit, conceptually similar to present-day standard 400-Hz aircraft alternators. The alternator incorpor-ates mechanical drive coupling provisions and electrical terminations. To provide the required AERL duty cycle, blast air cooling provisions will be added to the alternator. A 6.0-hp rating cooling fan motor assembly will be used. The final assembly will be determined during the proposed alternator program.

Major alternator parameters are summarized in Table D-1 and major dimensions of the alternator assembly are shown in Figure D-1. Alternator bearings are class 5 forced-oil-lubricated; oil is retained in the bearing cavities by carbon face seals located at both ends of each bearing. A roller bearing is used on the drive end, and a ball bearing is used on the opposite end. The machine form factor indicates that it is relatively long for its diameter and is representative of a low inertia and weight design. Length of the main alternator section of the machine is approximately 36 in. The remaining 17 in. of assembly length is for the ancillary exciters.

The impact of certain key power system parameters on alternator weight has been investigated on a preliminary basis using the 8-Mw alternator design as a baseline. One of the more important power system parameters to be con-sidered is output voltage. In this application, a relatively high (i.e., in the several thousand volts range) system and alternator output voltage is required. This high level of voltage requires, in turn, that a very high-quality insulation system be provided in the alternator. In the 8-Mw design, such an insulation system is intended and would be generically similar to the high-voltage and high-temperature systems used in present-day high-rating primary utility turboalternator equipment. Typically, these consist of corona-shielded, hot-pressed, void-free resin-bonded, high-quality flake mica insula-tion systems using preformed conductors rather than random or mush-wound coils as in smaller rating machines (e.g., aircraft generators). The thickness of the ground barrier insulation around the conductors in these high-voltage designs is significant and results in an appreciable volume for insulation relative to volume of conductor. In general, as the alternator voltage is increased and other machine parameters are maintained essentially constant, the amount of this insulation also must increase. Overall, the result is such that the proportion of alternator insulation to conductor volume decreases and alternator weight increases with increase of voltage.

TABLE D-1

MAJOR PARAMETER DESIGN SUMMARY, DC CASE

Parameter	Feature
Generated voltage (sinusoidal), L-N/L-L	8497/14,717
Speed, rpm	12500
Power factor (apparent)	0.878
Type	Nonsalient-pole, wound-field, synchronous, no damper
Frequency, Hz	416-67
Number of poles	4
Rotor peripheral velocity, ft/sec^2	597
Rotor moment of inertia, in.-lb-sec	26.67
Current loading, A/sq in.	
Stator	16318
Rotor	17799
Outside diameter, in.	19.8
Rotor diameter, in.	10.95
Active magnetic length, in.	24.0
Overall length, in.	53
Radial air gap length, in.	0.1
Efficiency (final), percent	96.0
Weight, lb	
Electromagnetic	1729
Controls/protection/exciters/ structure	569
Total	2298
Negative sequence reactance, per unit	0.31

Figure D-1 Alternator Assembly Outline

DIMENSIONS IN INCHES

TERMINAL BOX (SPANS 120°)

DRIVE END

22.3

16.5

12

14

S-398

53

36

19.8

20.3

20.0

4
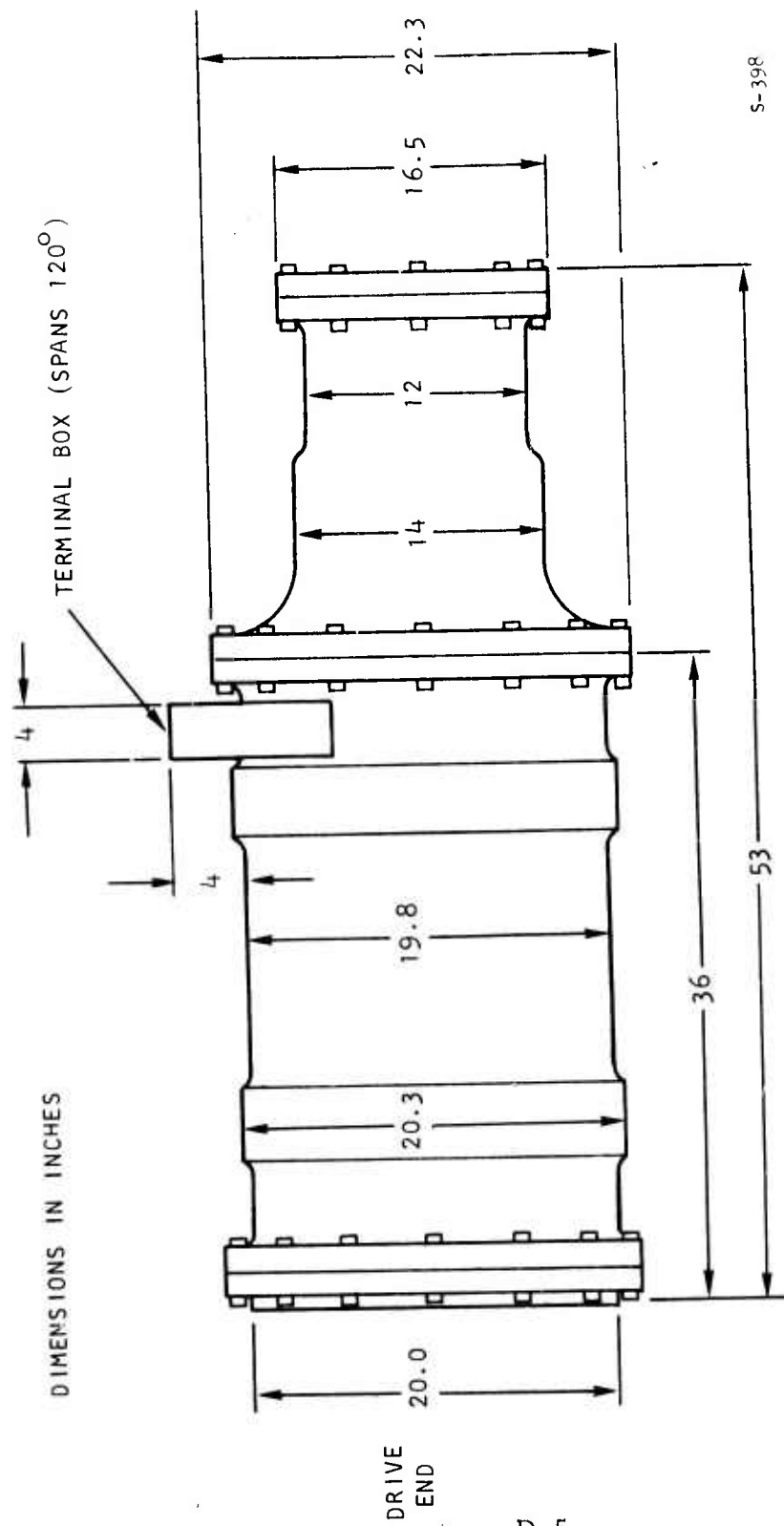
4

D-5

Figure 2 shows a plot of alternator total weight variation with power system output voltage for the 8-Mw design. The voltage plotted is average dc value for the 3-phase alternator, including the effects of a 0.31 per unit alternator negative sequence (i.e., cumulating) inductance on the rectification. The plot covers a 10 to 25 kvdc range, with the baseline voltage case being 17 kvdc.

Another key power systems parameter for consideration in regard to alternate weight impact is commutating inductance. This inductance normally is the sum of alternator (negative sequence) inductance, live inductances, and (if used) any transformer (leakage) inductance present on the input side of the rectifier circuits. The impact of increasing this reactance under conditions of rectified load is to increase the required kva rating of the alternator for a given kw output in much the same manner as under logging power factor or loading conditions. Such increased kva rating, of course, requires additional alternator weight; however, decreasing the value of alternator internal (negative sequence) inductance also has an adverse impact on alternator weight (i.e., as alternator inductance is made very low, alternator weight must significantly increase). Thus, the selection of alternator (and any attendant transformer and line) inductance to minimize the weight of a rectified output alternator is a tradeoff that may be further complicated by current overlapping in the rectifiers, voltage regulation and transient requirements, etc. These factors must be considered for the particular design. In most cases, it is useful to know the alternator weight versus percent inductance characteristics to make such a tradeoff. Figure D-3 presents such data for the 8-Mw design proposed.
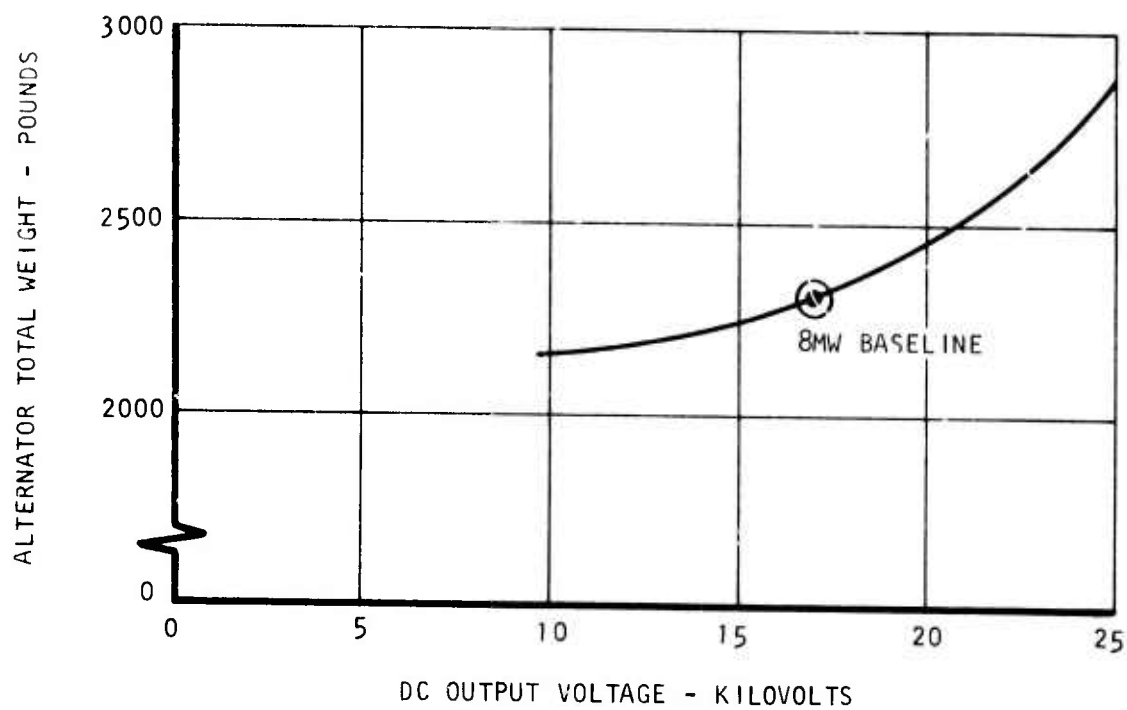
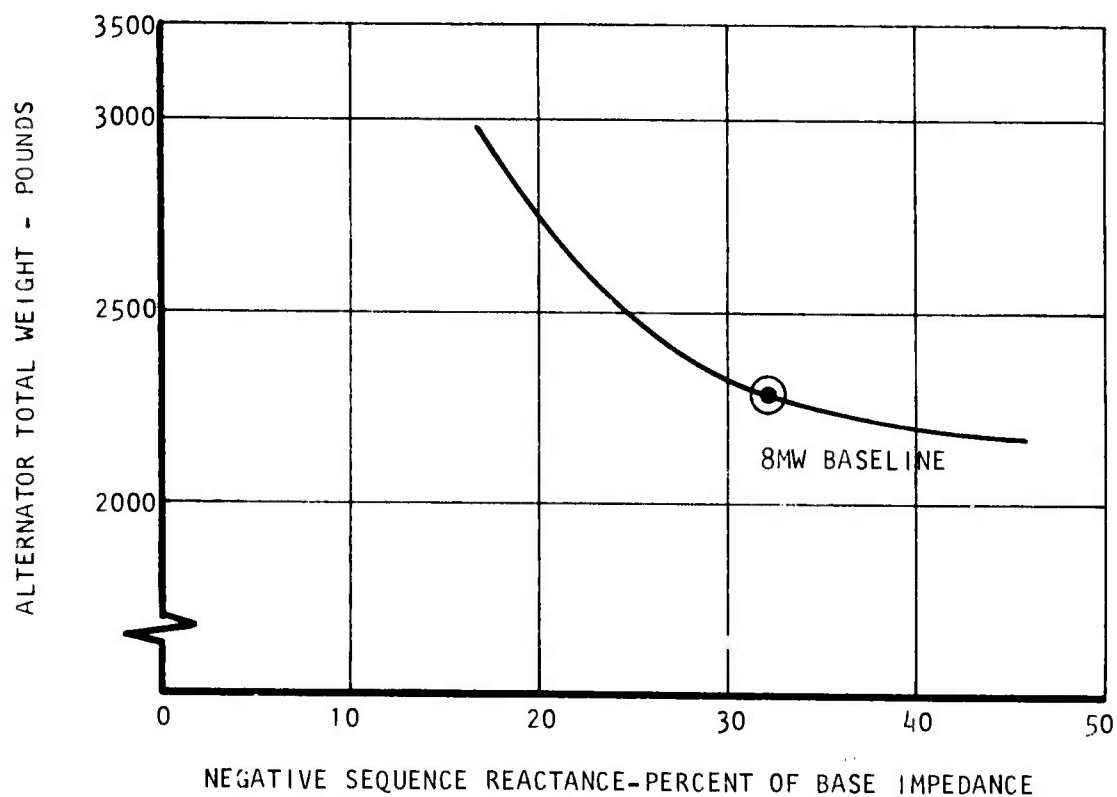**Figure D-2** Alternator Total Weight Vs Dc Output Voltage

Figure D-3 Alternator Total Weight Vs Alternator Reactance

APPENDIX E

PERFORMANCE AND CAPABILITIES ASSESSMENT, DUAL AXIS ANGLE STEERING MECHANISM
(RCA)

INTRODUCTION

Typical present day laser tracking applications require angle steering precision of 5 microradians or better. Until recently, angle steering precision of 50 to 100 microradians was considered the state-of-the-art for precision range instrumentation radars. This new precision requirement for lasers obviously required a new approach to angle steering. RCA has solved the problem by designing a very simple, multiple-gimbal, high-performance, fine-steering mechanism which has demonstrated -- under closed loop servo tests at 140 Hz bandwidth -- a precision better than 2 microradians with resolution better than 0.05 microradians.

An RCA IR&D program was started in June 1974 with a decision to design, fabricate, and test such a mechanism under closed loop servo control to prove out the angle steering performance of the RCA concept. The test program was completed in June 1975 with results that are considered a breakthrough in the precision of angle steering. By virtue of its simplicity and absence of wear-out phenomena, the device requires no maintenance or alignment. That it has an essentially unlimited operational life is in itself unique in the field of mechanisms. A photograph of the completed steering mechanism is shown in Figure E-1.

This mechanism was designed specifically for use in a High Energy Laser (HEL) Beam Director, to steer a 30 pound cooled metal mirror. Other applications for this mechanism are apparent, including an inertially stabilized version which can be used for precision electro-optic tracking, designating, surveillance, or data collecting systems.

A more detailed report, MTMR-75-TR-009, describing the RCA proprietary steering mechanism may be obtained by Government agencies upon request.
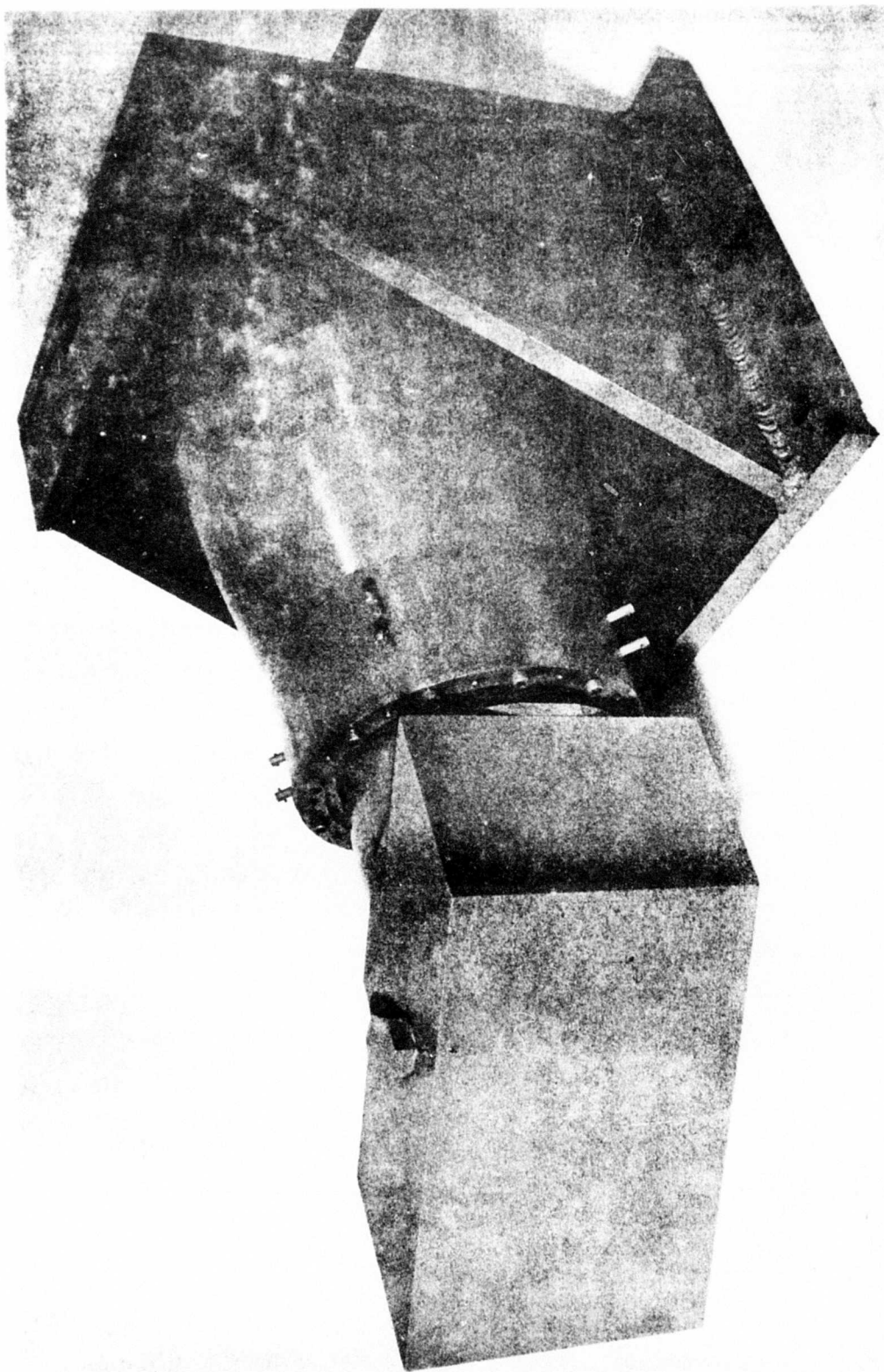
Figure E-1   Dual Axis Fine Steering Mechanism

MECHANISM

Achieving angle steering precision better than 5 microradians in any servoed mechanical device is dependent upon three critical mechanism parameters:

1. Any higher mode mechanical resonance must be greater than or at least equal to the required closed loop servo bandwidth. A lower mode resonance at frequencies below the bandwidth can be compensated by the servo.

2. To achieve high resolution, the mechanism must not exhibit lost motion or backlash.

3. Static friction (stiction or stick-slip) and hysteresis restraints must be minimized or eliminated. Linear viscous friction is desirable as a damping characteristic, though it is not really necessary in the RCA concept of damping through the servo loop. Static friction and hysteresis torques also provide damping; however, they are nonlinear and tend to degrade resolution and accuracy.

The RCA concept fulfills all three requirements and incorporates angle steering about two orthogonal axes in a compact package. In general the concept is limited to steering angles in the region of $\pm 0.5^{\circ}$ about each of the two axes, although coverage could be increased for other applications.

For the test program, the steered device consisted of a mass simulating the 30 pound water cooled mirror. The mirror orientation and steering mechanism outline are shown in Figure E-2. The size of the mechanism, of course, depends on the weight of the steered device as well as the offset from the steering axes to its center of gravity. The weight of the tested simulated steered mirror was 30 pounds, which when combined with the weight of other components, resulted in a total steered weight of 70 pounds. This weight ratio (70/30) would be expected to hold for other steered devices of similar offset between the center of gravity of the mirror and the intersection of the steering axes (5.25 inches for the 30 pound mirror). The weight of fixed components

ALL DIMENSIONS ARE IN INCHES

8 DIA

13

6

6¼ DIA

2½

5¼

STEERING AXES
INTERSECTION

STEERING
MECHANISM

ELEVATION
AXIS

STEERED
DEVICE

A

A

30 LB
MIRROR

45°

REFLECTED &
STEERED RAY

INCIDENT
RAY

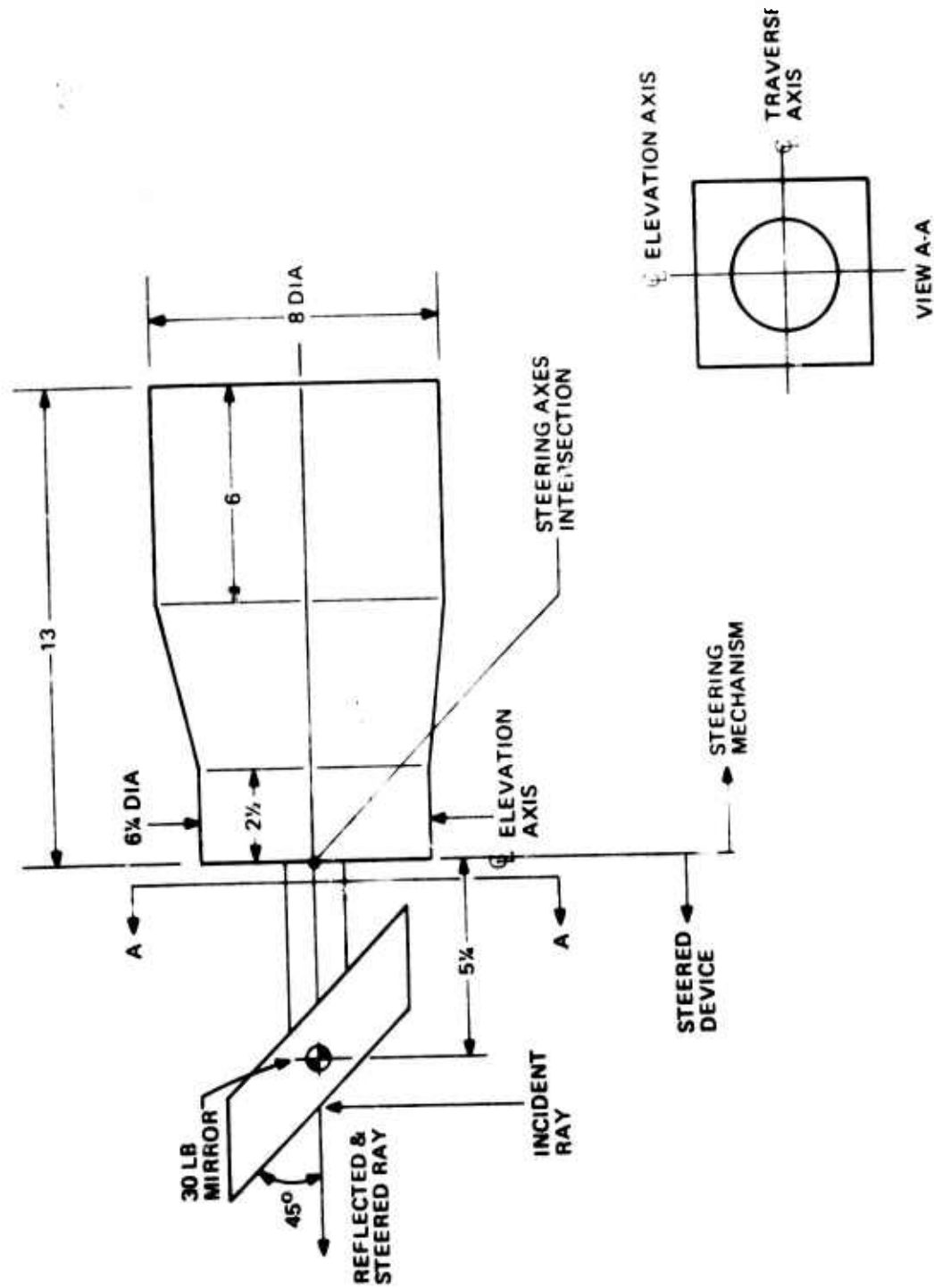ELEVATION AXIS

TRAVERSE
AXIS

VIEW A-A

Figure E-2 - Mechanism Outline

was 60 pounds making a total device weight of 130 pounds, which can be reduced for many other applications.

The mechanism volume requirement (excluding the steered device) is constrained by the weight of the steered device, by the angular acceleration required, and by the servo drive torque and power requirements. A given volume requirement can be satisfied by other mechanism length-to-diameter ratios (13/8 for the device tested, as shown in Figure E-2), with lower ratios preferred.

The usual inner/outer axis gimbal order and the attendant effects do not apply in this RCA design, Thus, rotation about one axis does not result in rotation of the second axis centerline.

SERVO

The mechanism is servoed by a dual axis electromagnetic actuator. The outer position servo loop closes through eddy-current pickoff sensors located on the gimbals. The actuator and pickoffs are non-contacting devices. A block diagram of the servo system is shown in Figure E-3. Five major criteria dictate the design of the servo system for the fine steering application:

1. The mechanism will be subject to a base vibration distrubance which is assumed to be random with a flat power spectral density (PSD) of 100 microradians RMS, bandlimited to 10 Hz. The isolation required is 34 dB or a reduction to 2 microradians RMS. This requirement sets the open loop gain needed and is well in excess of that needed for target tracking. In the laser application, the stabilization loop will be closed through either a rate integrating gyro sensor or an IR tracking sensor; however, for testing this prototype, the equivalent loop is implemented by the pickoff sensor. A Type 3 open loop with crossover at 56 Hz and pullup at 19 Hz satisfies the stabilization requirement. The resulting closed loop bandwidth is 110 Hz with 7 dB gain and 30° phase margins.
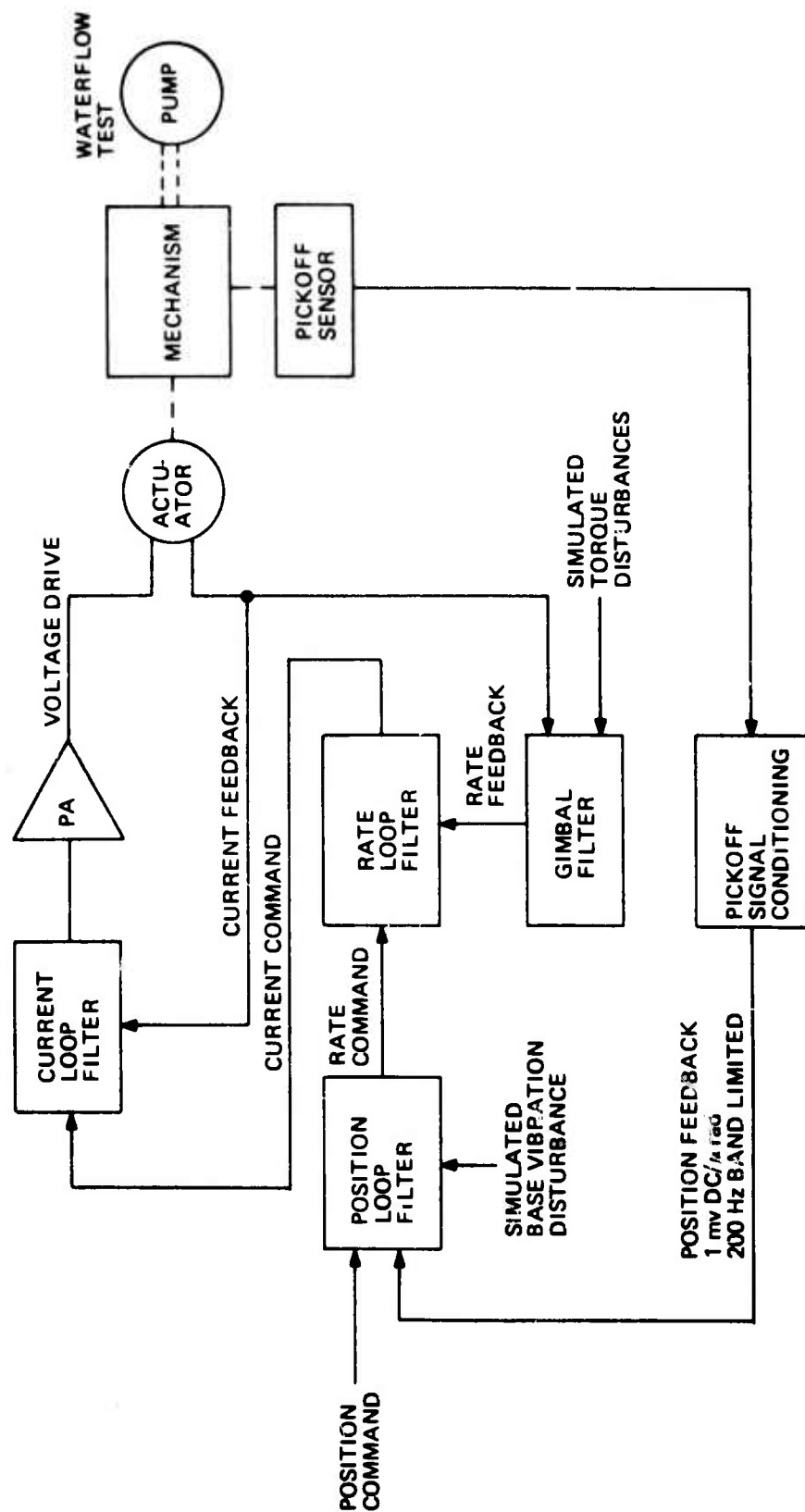
Figure E-3 Servo Block Diagram

2. A resolution (including repeatability and drift) of less than 1 microradian is required and is dependent on mechanism design (as previously described), tightness of the servo loop, and proper choice of sensor (pickoff).

3. Open loop gain and dynamic range must be compatible with a total noise equivalent input not to exceed 2 microradians RMS (200 Hz noise bandwidth) due to sensor noise and high frequency torque disturbances. This bounds the closed loop bandwidth to the 110 Hz value.

4. The servo drive torque and power (sizing) must be compatible with the large signal transient recovery acceleration needed for tracking and stabilization (the fine steering mirror must move for stabilization with optical transformation ratios other than unity) and non-saturated sinusoidal operation. The design requirements to attain this compatibility are 10 rad/sec^2 maximum acceleration, 3300 rad/sec^3 maximum jerk (rate of change of acceleration), and non-saturated sinusoidal operation of 10 microradians peak for frequencies up to the closed loop bandwidth. The jerk rating becomes the limiting factor in both sizing and sinusoidal saturation.

5. The position loop stiffness must be compatible with the open loop gain required for stabilization, in order to isolate torque disturbances that result from the waterflow associated with the mirror cooling. Tests have shown the waterflow torque disturbance to be 1.1 inch-pounds RMS (200 Hz noise bandwidth) and the isolation of this is compatible with maintaining the noise equivalent input below the 2 microradian (200 Hz noise bandwidth) level for operation at 110 Hz bandwidth.

As shown in Figure E-3, outer position loop closure is made through the position loop filter with simulated base vibration or positioning commands summed against the pickoff reference feedback signal. The position loop filter provides (1) two of the three loop integrations, (2) pullup compensation, and (3) bounding of position error and stored velocity and acceleration. The position loop filter output is a rate command to the rate loop filter. The

rate loop is synthetically developed from the gimbal filter (an idealized mechanism replica) and provides the third integration with mechanism compensation and damping and gimbal velocity bounding. The rate loop filter output is a current command to the current loop closure around the actuator. Simulated torque disturbances (see Figure E-3) are summed against current in the gimbal filter. The position loop closure is completed through the actuator driving the fine steering mirror which is sensed in position by the pickoff. The servo electronics are all analog utilizing $\mu747$ operational amplifier active filter and summing circuitry. The power amplifiers are linear complementary class B transistor design.

TEST RESULTS

The prototype angle steering mechanism was extensively tested under servo control over a six month period. A comparison of performance against design goals for various parameters is summarized in Tables E-1 and E-2. A photo of the mechanism and test electronics is shown in Figure E-4.

A summary of typical system noise errors to be expected is given in Table E-3, based on measurements with and without mirror cooling waterflow under closed loop servo control. There are no bias errors of any significance in this system, either theoretical or measured. The total noise error in Table E-3 is indicative of the precision of the system.

The test results indicate that all critical parameters were met, or bettered with significant margins in several areas such as bandwidth and resolution. The total measured noise error of less than 2 microradians (which is servo system dependent) leaves a comfortable margin for overall systems demanding accuracies of 5 microradians or better. This error is representative of the overall performance of the wide bandwidth stabilization loop required in laser applications. Although the water flow tests show degradation in resolution (due to hysteresis torque from the water lines) and increased noise error, this has little overall effect in the total noise error (as indicated in Table E-3).

TABLE E-1. MECHANISM AND ACTUATOR PERFORMANCE

Parameter	Units	Design Goal	Test Results
Gimbal Travel	mrad	± 6.25	± 8.0
Gimbal Velocity	mrad/sec	60	70
Acceleration	rad/sec^2	10	10.9
Jerk	rad/sec^3	3300	8300
Load Inertia	in-lb-sec^2	7.5	7.5
Load Resonance	Hz	280	550
Torque	in-lb max.	75	82
Current	amps max.	6.6	6.6
Stator Temp. Rise	$^{\circ}$F/watt	21	2
Power Supply Demand	Volt-amps max.	200	200
Current Loop Bandwidth	Hz	3200	10,000

Notes: 1. The maximum frequency at which measurements could be made under servo control was 350 Hz with no apparent resonances observed. The resonance measured by independent means was 550 Hz.

2. There was no apparent effect of backlash and restraining torque non-linearities based on resolution indicated in Table E-2 without water lines. The degradation in resolution with water lines was due to hysteresis torque of $\pm$ 0.055 in-lb measured over small torque levels.

3. Indicated 10,000 Hz current loop bandwidth applies to sense current feedback. Filtering between sense and actuator current limits the actuator current, and the actuator voltage noise transfer, to approximately 2,000 Hz bandwidth.

TABLE E-2. SERVO TYPE 3 POSITION LOOP PERFORMANCE

| Parameter	Units	Design Goal	Test Results
Open Pullup Frequency	Hz	19	19
Open Crossover Frequency	Hz	56	70
Closed -3 dB Bandwidth	Hz	110	140
Gain Margin	dB	7	11
Phase Margin	deg	30	39
Isolation to Flat PSD Bandlimited Noise Disturbances			
Base Vibration/10 Hz	μrad RMS/μrad RMS	0.02	0.015
External Torques/200 Hz	μrad RMS/in-lb RMS	1.2	0.9
Axis Cross Coupling Isolation at 10 Hz	dB	67	60
Resolution Including Repeatability and Drift			
Without Water Lines	μrad p-p	1.0	0.05
With Water Lines	μrad p-p	1.0	0.30

E-11
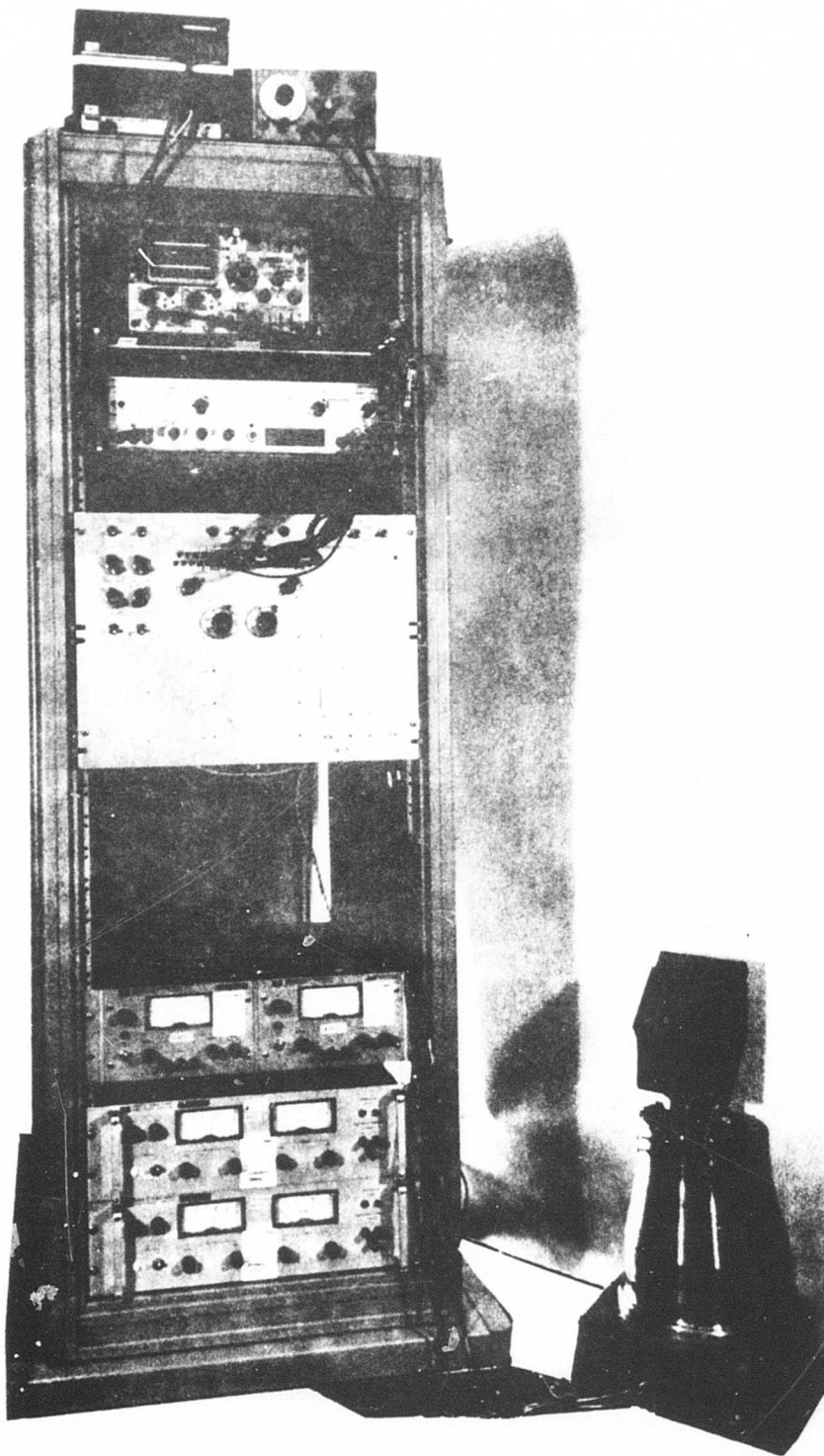
Figure E-4. Test Setup

E-12

TABLE E-3.   TYPICAL MEASURED SYSTEM NOISE ERRORS

Error Source (Noise Input)	Measured Noise (μrad RMS)	
	Without Water Lines	With Water Flow
Sensor (0.35 μrad RMS/200 Hz)	0.29	0.29
Resolution (0.05 & 0.3 μrad p-p)	0.02	0.09
Cross Coupling (100 μrad RMS/10 Hz)	0.1	0.1
Base Vibration (100 μrad RMS/10 Hz)	1.5	1.5
Water Flow (1.1 in-lb RMS/200 Hz)	0	1.0
Total RMS Noise Error (μrad)	1.53	1.83

Note: 1.   The sensor noise is that of the gimbal pickoff referred to 140 Hz band-
width and is used to present total system performance under simulated
conditions.   In an actual stabilization loop application, a gyro or track-
ing sensor would be used in place of the pickoff.

PERFORMANCE IMPROVEMENTS

The performance attained with this prototype steering mechanism is considered
excellent; the measured resolution of 0.05 microradians is significantly better
than the prior state-of-the-art.   The measured resolution demonstrates the very low
backlash and restraining torque non-linearities inherent in the RCA concept.

External electrical cabling or other service lines to the steered device will have an
impact on friction and hysteresis torques generated and therefore resolution.
Although these restraining torques (without backlash) may be tolerable in certain
circumstances, they must be minimized and controlled.

It was stated earlier that higher mode mechanism resonances must be at least equal
to the required servo bandwidth.   The design criterion for the prototype mechanical
resonance was 280 Hz minimum, allowing a 2 to 1 margin for the 110 - 140 Hz servo
bandwidth.   Measurements indicate that the limiting resonance was 550 Hz, thus the
existing design is not bandwidth limiting for servo bandwidths less than 280 Hz.

The bandwidth limiting resonance is defined by the dynamic characteristics of the steered device (mirror or other) as well as the mechanism design. This resonance can be increased by use of materials with a high specific modulus (the ratio of modulus of elasticity to density) such as beryllium rather than the all steel construction of the prototype. The electromagnetic actuator used in the prototype can be modified to achieve increased performance as discussed below.

The actuator was designed to achieve a peak torque of 75 in-lb; the measured value was 82 in-lb. Moreover, the actuator has a much better than expected thermal rise characteristic (2°F/watt versus 21°F/watt). Thus, the torque output can be approximately doubled without overheating. Incorporation of a simple and reliable cooling scheme within the existing actuator would permit a further torque increase.

The actuator can of course be redesigned in a larger size (larger mechanism diameter) to obtain increased torque. In addition to torque increases, it is desirable to reduce the load inertia. The prototype load inertia was 7.5 in-lb-sec^2 for the all steel construction. Reducing the offset between the center of gravity of the steered device and the steering axes, and the use of beryllium would significantly reduce the mass inertia. Increasing the actuator torque output and reducing mass inertia will increase angular acceleration capabilities, thus improving servo performance.

The potential of the existing actuator design for ⊾peration at higher bandwidths is shown in Table E-4. In this tabulation, only the actuator winding is changed for each bandwidth. The basic actuator and mechanism remains identical to the prototype.

The two parameters constraining increased servo bandwidth are power demand and noise saturation. Both of these parameters relate to dynamic range. Power demand or sizing, based on the design criterion of non-saturated sinusoidal operation at 10 microradians peak at the bandwidth frequency, increases with the fifth power of bandwidth or the product of maximum acceleration and jerk ratings. Jerk becomes the limiting parameter at higher bandwidths and is a function of actuator winding impedance and power supply voltage ratings.

TABLE E-4. SYSTEM REQUIREMENTS FOR INCREASED BANDWIDTHS

Parameter	Prototype BW 140 Hz	Projected BW	
		200 Hz	250 Hz
Crossover Frequency (Hz)	70	100	125
Inertia (in-lb-sec^2)	7.5	7.5	7.5
Acceleration (rad/sec^2)	10.9	20	24.7
Jerk (rad/sec^3)	8.3x10^3	24x10^3	48x10^3
Torque (in-lb max.)	82	150	185
Current (amps max.)	6.6	19.1	36.0
Torque Constant (in-lb/amp)	12.5	7.9	5.5
Power Supply Voltage (±volts DC)	30	50	60
Power Supply Demand (volt-amps max.)	200	960	2140
Total Allowable Noise Input Bandlimited to 3 X Crossover (µrad RMS max.)	1.1	0.6	0.4

Notes: 1. The total noise input is the broadband noise limit which will not cause noise saturation. This includes sensor noise and the residual from external high frequency torque disturbances. It excludes the residual from 100 microradians base vibration bandlimited to 10 Hz which at this frequency is narrowband noise and does not present a noise saturation problem; i.e., the noise transfer at 10 Hz is more than 40 dB down from the broadband noise at 3 x crossover for all three columns of the table.

As indicated in Table E-4, it takes a large power supply increase (from 200 to 2140 volt-amps with a 2 to 1 increase in power supply voltage) for a relatively small increase in bandwidth (from 140 to 250 Hz). A 2140 volt-amp rating is considered an upper limit for conventional linear power amplifier designs.

Noise saturation increases with the third power of bandwidth for a given total noise input bandlimited to 3 X crossover frequency. The noise saturation limit increases proportionally with power supply voltage. As indicated in Table E-4, operation at 140 Hz bandwidth appears to be the limit in view of the fact that present state-of-the-art gyro and tracking sensors are 1.0 microradian RMS noise devices when bandlimited to 3 X crossover or approximately 200 Hz. Noise from these sensors combined with external torque noise would exceed the total noise input given in Table E-4 at 140 Hz bandwidth, causing noise saturation. Operation at 140 Hz under these noise conditions would then require changing winding impedance and power supply voltage for compatibility with the values indicated under the 200 Hz column in Table E-4.

Thus the basic design is able to support a 250 Hz bandwidth in a low noise environment, provided actuator windings and sizing are revised in accordance with Table E-4. Considering the practical noise environment, compatible operation is constrained to bandwidths between 140 and 200 Hz.

CONCLUSIONS

The prototype tests were successful in verifying the design concept and demonstrating performance well beyond expectations.

The performance can be further improved by use of larger actuators and by using beryllium rather than steel. However, such performance increases are of no real value unless system noise is reduced as bandwidth is increased. The design as tested at 140 Hz bandwidth is considered adequate for sensor noise levels attainable at the present time. As sensors become available in the future at reduced noise, then compatible operation at higher bandwidths can be accomplished with redesign.

The mechanism is adaptable to provide an inertially stabilized line-of-sight for precision electro-optic tracking sensors, as well as other uses. Such a mechanism is now under development.